

## PAPER

[View Article Online](#)  
[View Journal](#) | [View Issue](#)
Cite this: *Nanoscale*, 2024, **16**, 21317

# Tunable $\text{Zn}^{2+}$ de-solvation behavior in $\text{MnO}_2$ cathodes *via* self-assembled phytic acid monolayers for stable aqueous Zn-ion batteries†

 Tianhang Ding,<sup>‡a,b</sup> Shichao Yu,<sup>‡a,c</sup> Ziyu Feng,<sup>a</sup> Bin Song,<sup>\*d</sup> Hong Zhang<sup>id</sup><sup>\*c</sup> and Ke Lu<sup>id</sup><sup>\*a,b</sup>

Sluggish ion diffusion kinetics at the electrode/electrolyte interface leads to insufficient rate capability and poor structural reversibility, which are mainly attributed to the hydrated  $\text{Zn}^{2+}$  migration process being inhibited due to its huge de-solvation energy barriers. Herein, a self-assembly method is proposed in which a multifunctional monolayer with phytic acid (PA) is coated on the surface of  $\text{MnO}_2$  strongly attaching to the substrate with the formation of chemical bonding to effectively prevent the dissolution of PA in the electrolyte. Due to the negative charge and inherent ultra-hydrophilicity of PA, modified  $\text{MnO}_2$  demonstrates stronger adsorption of positive ions and captures reactive water molecules, easily accelerating the de-solvation process of interfacial hydrated  $\text{Zn}^{2+}$ , efficiently achieving reversible  $\text{Zn}^{2+}$  insertion/extraction. Meanwhile, the coating layers can protect the substrate from attack by active water molecules, thus inhibiting cathode dissolution during battery cycling. Experimental characterization studies reveal that the protected  $\text{MnO}_2$  cathode exhibits a remarkable specific capacity of  $273 \text{ mA h g}^{-1}$  with a zinc intercalation capacity contribution of more than 60% at a current density of  $0.1 \text{ A g}^{-1}$ . Additionally, even at a high current density of  $1 \text{ A g}^{-1}$ , it maintains a capacity of  $197 \text{ mA h g}^{-1}$ , far exceeding that of pure  $\text{MnO}_2$ . Furthermore, the Zn-ion pouch cell, serving as a proof of concept, achieves an impressive energy density of  $300 \text{ W h kg}^{-1}$  and exhibits remarkable capacity retention of 77% even after 100 cycles. This work offers a universal strategy for expediting the de-solvation process of hydrated  $\text{Zn}^{2+}$  on the surface of manganese-based cathodes in aqueous zinc-ion batteries.

Received 5th September 2024,

Accepted 16th October 2024

DOI: 10.1039/d4nr03635b

[rsc.li/nanoscale](https://rsc.li/nanoscale)

## Introduction

Low cost and improved safety have gradually become the primary considerations in the field of energy storage; in this context, aqueous zinc-ion batteries stand out as the most promising alternative technology.<sup>1–6</sup> Various cathode materials have been developed for aqueous Zn batteries, including manganese-based oxides, vanadium-based oxides, Prussian blue analogs, and organic compounds.<sup>7–11</sup> Among them,

$\alpha\text{-MnO}_2$  with a  $2 \times 2$  tunnel structure, serving as a non-toxic and versatile cathode, holds significant potential.<sup>12–16</sup> Additionally, the theoretical energy density of the Zn/ $\text{MnO}_2$  system exceeds  $250 \text{ W h kg}^{-1}$ , comparable to the theoretical energy density of commercial lithium-ion batteries ( $200\text{--}300 \text{ W h kg}^{-1}$ ).<sup>17–21</sup>

However, severe capacity degradation, low discharge capacity, and poor cycling reversibility hamper the advancement of Zn/ $\text{MnO}_2$  batteries.<sup>22–25</sup> In particular, the low proportion of the capacity contributed to by zinc-ion (de)intercalation during the cycling process hinders the full exploitation of the Zn/ $\text{MnO}_2$  cell's performance.<sup>26–29</sup> Furthermore, zinc ions in solution typically exist in the form of hexa-coordinated complexes with water molecules.<sup>30–32</sup> During discharge, the insertion of zinc ions with water sheaths into the cathode electrode material can easily disrupt the structure of the cathode electrode material, reducing battery lifespan.<sup>33–35</sup> Moreover, the introduction of water molecules can lead to irreversible side reactions, resulting in the loss of active materials and causing significant capacity decay.<sup>36–38</sup> To overcome these obstacles, surface-coating strategies have been proposed to alter the elec-

<sup>a</sup>Institutes of Physical Science and Information Technology, School of Materials Science and Engineering, Anhui University, Hefei, Anhui 230601, China. E-mail: [luke@ahu.edu.cn](mailto:luke@ahu.edu.cn)

<sup>b</sup>State Key Laboratory of Polymer Materials Engineering, Sichuan University, Chengdu, Sichuan 610065, China

<sup>c</sup>School of Chemistry and Chemical Engineering, Harbin Institute of Technology, Harbin, Heilongjiang 150001, China. E-mail: [zhanghonghit@hit.edu.cn](mailto:zhanghonghit@hit.edu.cn)

<sup>d</sup>Institute of Functional Nano & Soft Materials (FUNSOM), Soochow University, Suzhou, Jiangsu 215123, China. E-mail: [bsong@suda.edu.cn](mailto:bsong@suda.edu.cn)

†Electronic supplementary information (ESI) available. See DOI: <https://doi.org/10.1039/d4nr03635b>

‡These authors contributed equally to this work.

trode–electrolyte interface chemistry as a way of facilitating the transfer of electrons and ions at the electrode surface and prohibiting side reactions.<sup>39–41</sup> By adjusting suitable hydrophilic or hydrophobic interfacial layers, the de-solvation behavior of zinc ions can be accelerated, promoting faster migration rates of water-sheath-free zinc ions and facilitating zinc intercalation, thus enhancing stability.<sup>42,43</sup>

In this study, we present a novel approach to modify the interface of  $\text{MnO}_2$  by utilizing self-assembled phytic acid. Through chemical bonding, the PA molecules strongly attach to the substrate, preventing PA from dissolving in the electrolyte. The modified layer can enhance the adsorption of positive ions and facilitate the de-solvation process of interfacial hydrated  $\text{Zn}^{2+}$ . This modification not only enables efficient reversible  $\text{Zn}^{2+}$  insertion/extraction but also protects against the attack of active water molecules, thereby preventing cathode dissolution during battery cycling. Experimental characterization studies demonstrate that the protected  $\text{MnO}_2$  cathode exhibits an impressive specific capacity of 273 mA h  $\text{g}^{-1}$ , with the zinc intercalation capacity contributing more than 60% at a current density of 0.1 A  $\text{g}^{-1}$ . Additionally, the proof-of-concept Zn-ion pouch cell attains a high energy density of 300 W h  $\text{kg}^{-1}$  and retains 77% of its capacity after 100 cycles.

## Results and discussion

### Structural characterization of self-assembled $\text{MnO}_2$ @PA nanowires

As illustrated in Fig. 1a, pristine  $\text{MnO}_2$  nanofibers were fabricated through a hydrothermal reaction. The  $\text{MnO}_2$  was then immersed in phytic acid (PA) solution and the PA functional film was chemically attached to the  $\text{MnO}_2$  surface via spontaneous completion of a self-assembly process. The ESI (Fig. S1 and S2†) provides details on the determination of PA concentration and dosage. The effect of the coating layer on

$\text{MnO}_2$  was further elucidated through scanning electron microscopy (SEM) and X-ray diffraction (XRD) (Fig. S3 and S4†). These analyses revealed that the macroscopic structure of the nanorods remains discernible, and all diffraction peaks can be accurately indexed to the phase-pure  $\alpha\text{-MnO}_2$  (standard JCPDS 44-0141). This result proved that the flexible film coating did not damage its crystal structure. The microstructure of the sample was revealed through transmission electron microscopy (TEM) imaging (Fig. 1b and c). In comparison with  $\text{MnO}_2$  samples (Fig. 1b) with clear lattice stripes, the surface of  $\text{MnO}_2$ @PA (Fig. 1c) appeared blurred, indicating that the rod-like manganese oxide surface was coated with a thin film. Moreover, the thickness of the layer was determined by the linear energy dispersive X-ray (EDX) spectroscopy scan (Fig. 1d), yielding a measurement of approximately 3–4 nm. Subsequently, the energy dispersive X-ray (EDX) spectroscopy image is shown in Fig. 1e, which confirmed the presence of elemental P on the  $\text{MnO}_2$ @PA material. Fig. 1f further demonstrates the uniform distribution of manganese (Mn), oxygen (O), and phosphorus (P) elements through transmission electron microscopy elemental mapping. Additionally, the distribution of the P element along the primary structure of the nanorods indicated the effective encapsulation of the film around the  $\text{MnO}_2$ . In order to obtain the bound state between the phytic acid layer and the  $\text{MnO}_2$  matrix, the X-ray photoelectron spectroscopy (XPS) survey spectra of the pristine  $\text{MnO}_2$  and  $\text{MnO}_2$ @PA were recorded. As depicted in Fig. 1g, the 2p orbital of phosphorus (P) in  $\text{MnO}_2$ @PA exhibits a diffraction peak at a binding energy of 132.9 eV, indicating the presence of a P–O–Mn bond on the surface of the  $\text{MnO}_2$ @PA nanowires. Meanwhile, Fig. 1h presents the high-resolution O 1s XPS spectra, where the appearance of a peak for P–O–Mn (531.2 eV) in the O 1s spectrum of  $\text{MnO}_2$ @PA further substantiated that the PA molecule exists in a chemically bonded state with  $\text{MnO}_2$ . Predictably, this film has excellent stability due to the presence of a P–O–Mn chemical bond. This result was further verified by an electrode immersion experiment (Fig. S5†) without major fluctuations in pH value after 3 days of the  $\text{MnO}_2$ @PA electrode being immersed in 2 M  $\text{ZnSO}_4$  electrolyte.

### The strong adsorption and the de-solvation process of zinc ions at the electrolyte/cathode interface

The investigation of zeta potential can provide valuable insights into the unique adsorption characteristics of various ions at the interface. As demonstrated in Fig. 2a, the pristine  $\text{MnO}_2$  sample reveals a negatively charged surface with a zeta potential of −4.2 mV. Obviously, the self-assembly of PA with its strong negative charge on the  $\text{MnO}_2$  substrate resulted in a significant negative shift in zeta potential (−6.3 mV), implying that the interface of  $\text{MnO}_2$ @PA can adsorb positive ions more strongly and facilitate a more rapid storage process. Furthermore, additional charges that were adsorbed at the interface may lead to an increase in the interfacial capacitance, which was further investigated by the analysis of differential capacitance, as depicted in Fig. 2b. In particular, a notable



Ke Lu

*Ke Lu is currently a full professor at Anhui University, Hefei, China. He received his Ph.D. from Shandong University in 2018. During 2017–2018, he worked as a visiting PhD student at the Institute of New Energy for Vehicles at Tongji University, under the supervision of Prof. Yunhui Huang. Prior to his current position, Ke worked as a postdoctoral researcher at Northern Illinois University and Argonne National Laboratory*

*(2018–2020). He has published more than 90 peer-reviewed papers with an H-index of 34. His group works in electrochemistry and related applications.*

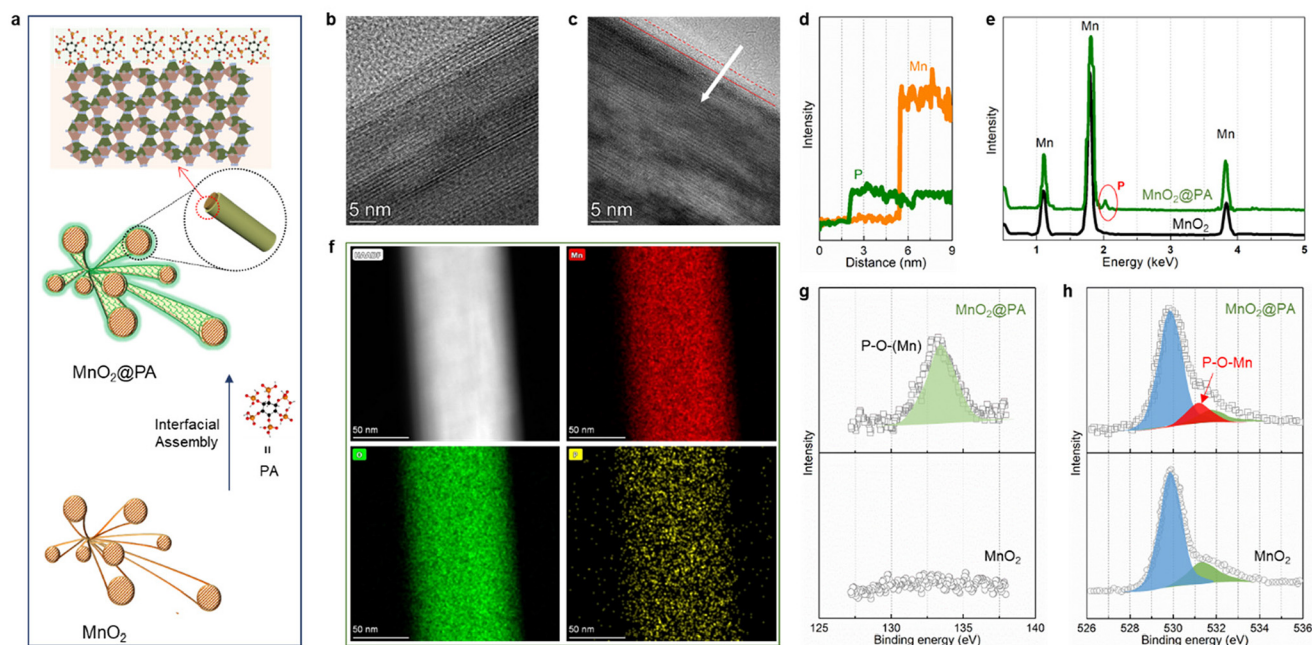


**Fig. 1** Structural and morphological characteristics of MnO<sub>2</sub>@PA nanofibers. (a) Schematic illustration of the synthesis of MnO<sub>2</sub>@PA; transmission electron microscopy images of (b) pure MnO<sub>2</sub> and (c) MnO<sub>2</sub>@PA; (d) linear EDX scan of the elements and (e) EDX image of MnO<sub>2</sub>@PA; (f) HAADF-STEM and corresponding elemental mappings of MnO<sub>2</sub>@PA; XPS spectra of (g) P 2p and (h) O 1s for MnO<sub>2</sub>@PA and pristine MnO<sub>2</sub>.

positive shift in the potential of zero charge (PZC) is observed on the MnO<sub>2</sub>@PA surface.<sup>39</sup> These results can be attributed to the strong specific adsorption of cations at the interface, further confirming that the PA coating could enhance the attraction of the interface to insertion ions.

Moreover, the contact angle of the loaded active substance cathode sheet was tested (Fig. S6†). It is clear that the contact angle of the MnO<sub>2</sub>@PA cathode was significantly smaller than that of the pristine MnO<sub>2</sub>, demonstrating that the modified layer could improve the cathodic hydrophilicity. Thus, the modified film is expected to trap water molecules, thereby facilitating the de-solvation process of Zn(H<sub>2</sub>O)<sub>6</sub><sup>2+</sup> at the interface.<sup>44–47</sup> To validate this assumption, the enhanced Zn<sup>2+</sup> de-solvation of MnO<sub>2</sub>@PA cathodes can be effectively assessed by evaluating the activation energy ( $E_a$ ) from Nyquist plots at various temperatures, as shown in Fig. 2c. In addition, the  $E_a$  profiles at various voltages for the MnO<sub>2</sub> and MnO<sub>2</sub>@PA cathodes are shown in Fig. 2d. On the whole,  $E_a$  of MnO<sub>2</sub>@PA was lower than that of MnO<sub>2</sub> throughout the discharge phase, suggesting that this modified film is beneficial for reducing the energy barrier of ion transfer. In particular, in the Zn<sup>2+</sup> interpolation-dominated section (about 1.4–1.0 V), the pristine MnO<sub>2</sub> cathode had a very high de-solvation barrier and energy, in contrast to that with the coating of the PA layer, which considerably alleviates the de-solvation potential. In summary, the outcome demonstrated a notable acceleration in the de-solvation process of hydrated Zn<sup>2+</sup> and an improvement in the insertion kinetics of Zn<sup>2+</sup> by the PA layer.

Additionally, the strong interaction between the water sheath and the PA layer alters the original chemical force. To

support the Zn<sup>2+</sup> pre-de-solvation effect of the PA layer, Fourier transform infrared (FT-IR) spectra were employed. As shown in Fig. 2e, after immersing the MnO<sub>2</sub>@PA cathode in 2 M ZnSO<sub>4</sub>, the H-bond wavenumber value decreased, indicating that the strong affinity of the PA interface for the water sheath elongates the H-bond length. Additionally, Raman spectroscopy was used to examine the solvation structure of Zn<sup>2+</sup>. As depicted in Fig. 2f, the peak position of the  $\nu$ -SO<sub>4</sub><sup>2-</sup> band shifted to a higher frequency within the PA interface, suggesting that Zn<sup>2+</sup> is tightly bound to SO<sub>4</sub><sup>2-</sup> anions due to the removal of the water sheath. Fig. 2g and h intuitively display the de-solvation behavior of zinc ions at the interface layer. The gradual approach of hydrated zinc ions towards the positive electrode surface, owing to the negative charge potential of the cathode, prompted some of these ions to undergo de-solvation. The incorporation of the PA layer notably diminishes the de-solvation barrier, facilitating the intercalation of more zinc ions. Additionally, this modified layer exhibited exceptional hydrophilicity, effectively shielding the MnO<sub>2</sub> matrix from the corrosive effects of activated water post-de-solvation. In conclusion, the modification layers can promote the de-solvation of hydrated zinc ions, accelerate the transport kinetics of zinc ions, and increase the electrochemical capacity.

### The functional coated layer directs stable Zn<sup>2+</sup> (de)insertion

To study the effect of the modification layers on electrochemical efficiency, the performance of a modified MnO<sub>2</sub> cathode material was evaluated through a series of electrochemical tests on MnO<sub>2</sub>@PA and MnO<sub>2</sub> electrodes. The charge



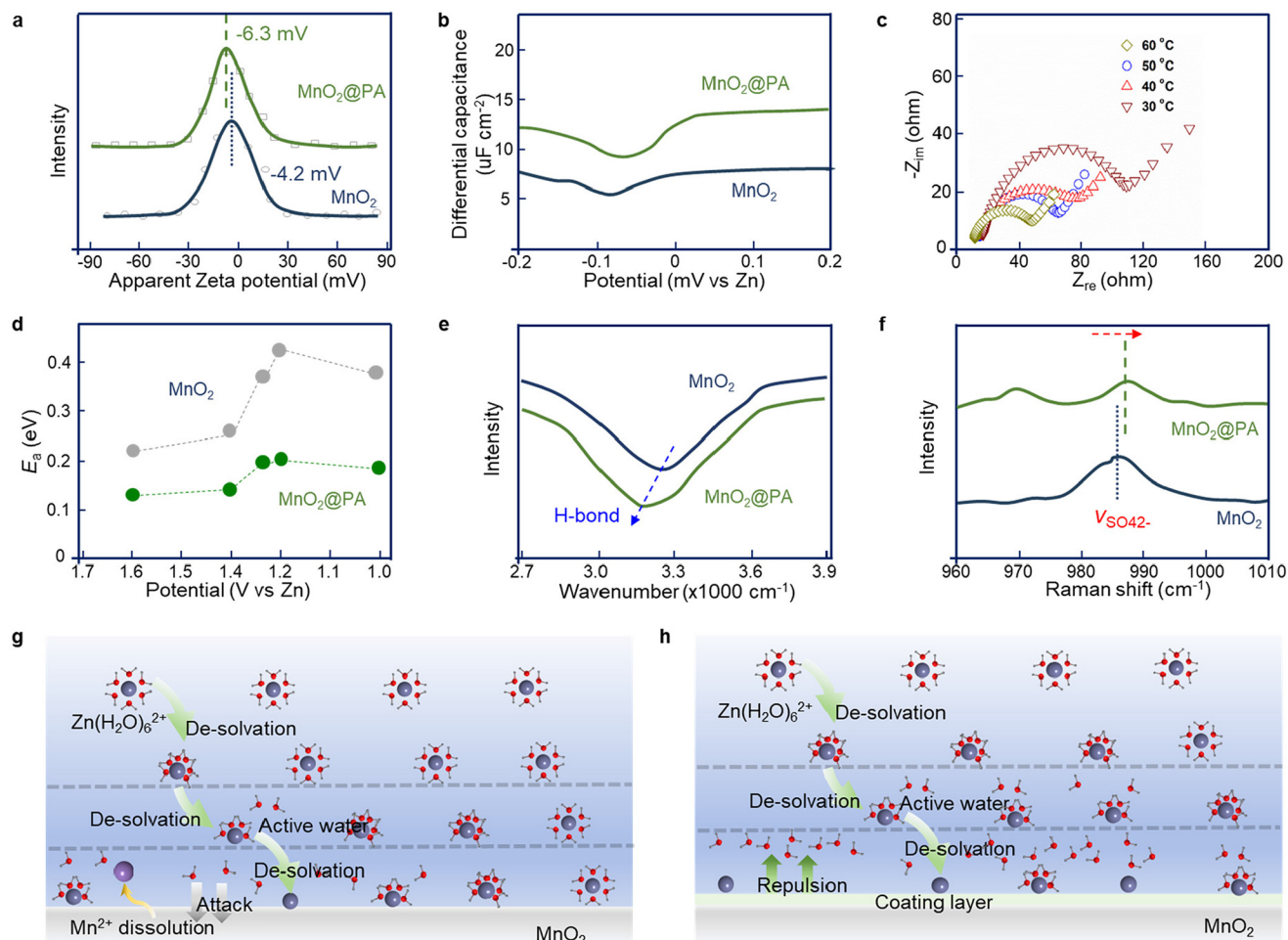


**Fig. 2** Adsorption and de-solvation behavior of zinc ions at the interface layer. (a) Zeta potential of MnO<sub>2</sub> and MnO<sub>2</sub>@PA cathodes. (b) The differential capacitance–potential curves of MnO<sub>2</sub>@PA electrodes. (c) Nyquist plots for MnO<sub>2</sub>@PA at various temperatures. (d) The calculated Zn<sup>2+</sup> de-solvation energy of bare MnO<sub>2</sub> and MnO<sub>2</sub>@PA electrodes. (e) Fourier transform infrared (FT-IR) spectra of H-bonds in MnO<sub>2</sub> and MnO<sub>2</sub>@PA immersed in 2M ZnSO<sub>4</sub>. (f) Raman spectroscopy of SO<sub>4</sub><sup>2-</sup> in MnO<sub>2</sub> and MnO<sub>2</sub>@PA immersed in 2 M ZnSO<sub>4</sub>. Schematic diagram of de-solvation behavior in (g) MnO<sub>2</sub> and (h) MnO<sub>2</sub>@PA electrodes.

and discharge curves are depicted in Fig. 3a, revealing that the MnO<sub>2</sub>@PA cathode has a preferable specific capacity of 273 mA h g<sup>-1</sup>, significantly outperforming the MnO<sub>2</sub> cathode (158 mA h g<sup>-1</sup>) under a low current density of 0.1 A g<sup>-1</sup>. Impressively, the pure MnO<sub>2</sub> exhibits an obvious potential difference with respect to electrochemical behavior when changing from insertion of H<sup>+</sup> to the insertion of Zn<sup>2+</sup> (Fig. 3b). Previous studies have indicated that the large molecular size of hydrated zinc ions hinders their reversible insertion into the manganese dioxide lattice, and thus this phenomenon results in a reduced intercalation capacity during the second phase of the pristine MnO<sub>2</sub> as well as to a large potential difference during the transition of the dominant intercalation ions. In contrast, the interfacially modified MnO<sub>2</sub> exhibits smooth electrochemical transition behavior, suggesting that the modified layer significantly improved the intercalation kinetics at the Zn<sup>2+</sup> insertion (region II). To determine the capacity contribution of Zn<sup>2+</sup> insertion, it is essential to precisely quantify

the proportion of H<sup>+</sup> intercalation capacity. For this purpose, coin batteries were assembled using 0.2 M MnSO<sub>4</sub> as the electrolyte. Since there is no Zn<sup>2+</sup> in the electrolyte, the H<sup>+</sup> intercalation capacity can be quantitatively obtained. Fig. 3c and d show that the capacities of the insertion of H<sup>+</sup> in MnO<sub>2</sub> and MnO<sub>2</sub>@PA cathodes are 87.6 and 101 mA h g<sup>-1</sup> at a current density of 0.1 A g<sup>-1</sup>, respectively. In other words, the capacity contribution of Zn<sup>2+</sup> insertion in the MnO<sub>2</sub>@PA cathode is 63.2%, much higher than the capacity share of 44.5% in the MnO<sub>2</sub> cathode. Moreover, the capacity contributions of Zn<sup>2+</sup> insertion in the MnO<sub>2</sub>@PA cathode at all current densities are collected (Fig. 3e). In particular, the Zn intercalation capacity of the modified cathode decays by only 13.2% when the current density is increased by a factor of 10 and the charge/discharge curves are evident, demonstrating fast interfacial ion transport/reaction kinetics. Fig. 3f illustrates that the MnO<sub>2</sub>@PA cathode demonstrates a significant Zn<sup>2+</sup> insertion capacity exceeding 50% at all current densities. This obser-

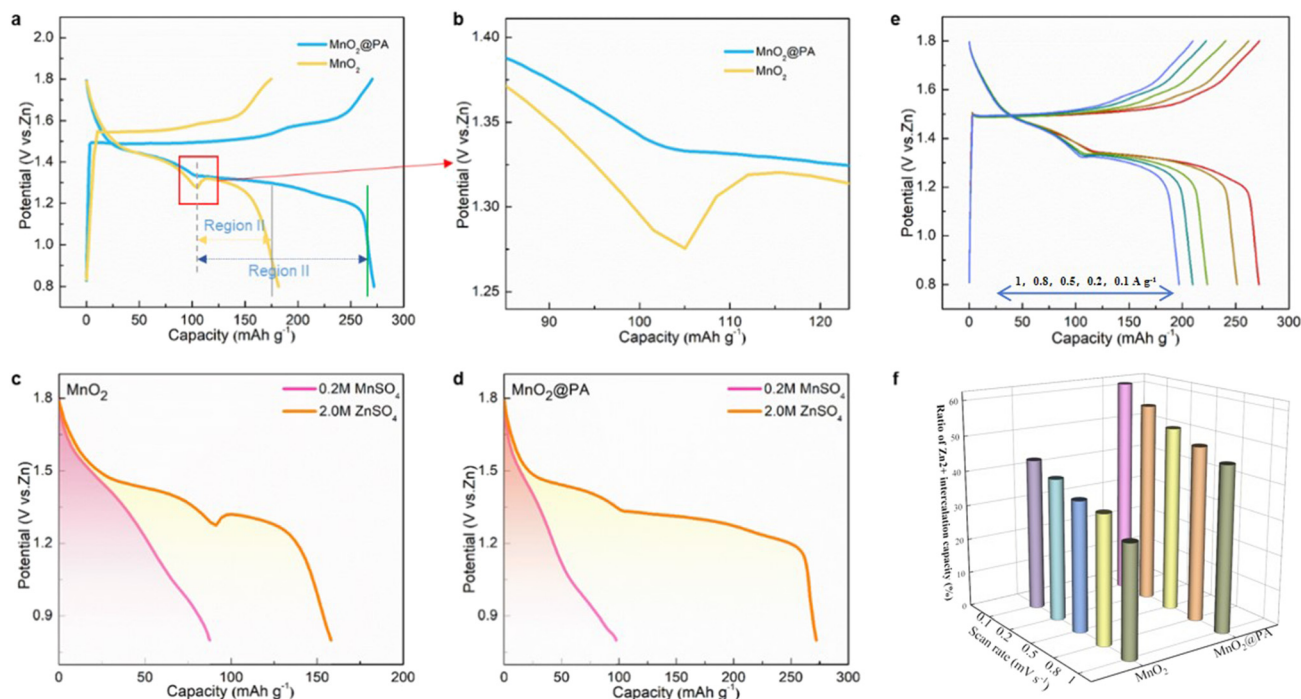


**Fig. 3** The electrochemical performances of Zn-MnO<sub>2</sub> batteries. (a) Charge–discharge curves of MnO<sub>2</sub>@PA and pure MnO<sub>2</sub> cathodes at 0.1 A g<sup>−1</sup>. (b) The highlighted activation behaviors for the reduction shown in (a) are magnified. The discharge curves of (c) MnO<sub>2</sub> and (d) MnO<sub>2</sub>@PA at 0.1 A g<sup>−1</sup> in different electrolytes. (e) Charge–discharge profiles of MnO<sub>2</sub>@PA collected at different current densities. (f) The capacity of Zn<sup>2+</sup> insertion of MnO<sub>2</sub>@PA and MnO<sub>2</sub> at all current densities.

vation indicates that the modified MnO<sub>2</sub>@PA cathode plays a crucial role in enhancing the intercalation capacity of Zn<sup>2+</sup>, ultimately leading to a higher overall capacity being achieved.

### Optimized cation intercalation kinetics

The improved redox kinetics in altered MnO<sub>2</sub> electrodes was additionally verified through cyclic voltammetry (CV) analysis (Fig. 4a). It is worth mentioning that MnO<sub>2</sub> cathodes modified with PA displayed increased redox currents and narrower cathodic–anodic peak separations in comparison with the original MnO<sub>2</sub> cathode. This indicates that the surface modification has resulted in enhanced ion storage capacity and more robust kinetics. In particular, the height and area of the second reduction peak (1.29 V) for MnO<sub>2</sub>@PA far exceed those for pure MnO<sub>2</sub>, which corresponds to the Zn insertion process. This difference could be attributed to the smaller ionic volume of de-solvated Zn ions, which is very favorable for their intercalation process and is consistent with the significantly enhanced Zn insertion capacity in the constant-current charge/discharge test. The ion diffusion dynamics in different cathodes was quantified by CV measurements at increasing scan rates (Fig. 4b and S7†). As depicted in Fig. 4c, utilizing analysis of the Randles–Sevcik relationship, a linear correlation exists between the square root of the scan rate and the anodic peak current, and this linear correlation indicates a diffusion-limited electrochemical process, with the slope directly related to the ion diffusion coefficient.<sup>33</sup> The slope of the modified MnO<sub>2</sub> consistently exceeds that of pure MnO<sub>2</sub>,

demonstrating that the modification layer can enhance ion transport efficiency. To further quantify the ion diffusion kinetics of the samples, galvanostatic intermittent titration technique (GITT) measurements were conducted. Fig. 4d and e display the voltage profiles of MnO<sub>2</sub> and MnO<sub>2</sub>@PA recorded during the GITT evaluation. The results presented in Fig. 4f and S8† indicate a higher diffusion coefficient for the coated MnO<sub>2</sub> sample during battery operation, elucidating the accelerated ion diffusion in MnO<sub>2</sub>@PA. Notably, the ion diffusion coefficient has a significant decrease when the pure MnO<sub>2</sub> discharge process is converted from H-insertion to Zn-insertion dominance in the second loop discharge stage. In contrast, the modified positive electrode has a higher *D* value for the full discharge process. This result can be attributed to the de-solvated Zn<sup>2+</sup> entering the manganese dioxide lattice more easily, leading to a faster ion transport rate during the reduction process.

### Investigations of the degradation mechanism and cycling performance

We further investigated the decay mechanism of the battery and characterized the electrode after cycling. The cathodic degradation mechanism is delineated in Fig. 5a and b. Post-cycling tests, as depicted in Fig. 5a, reveal that the morphology of the modified MnO<sub>2</sub> cathodes remains intact even after 100 cycles, indicating that the coated layer confers high structural integrity upon the treated substrate. In stark contrast, the structure of MnO<sub>2</sub> evolves from its original nanofibers to a

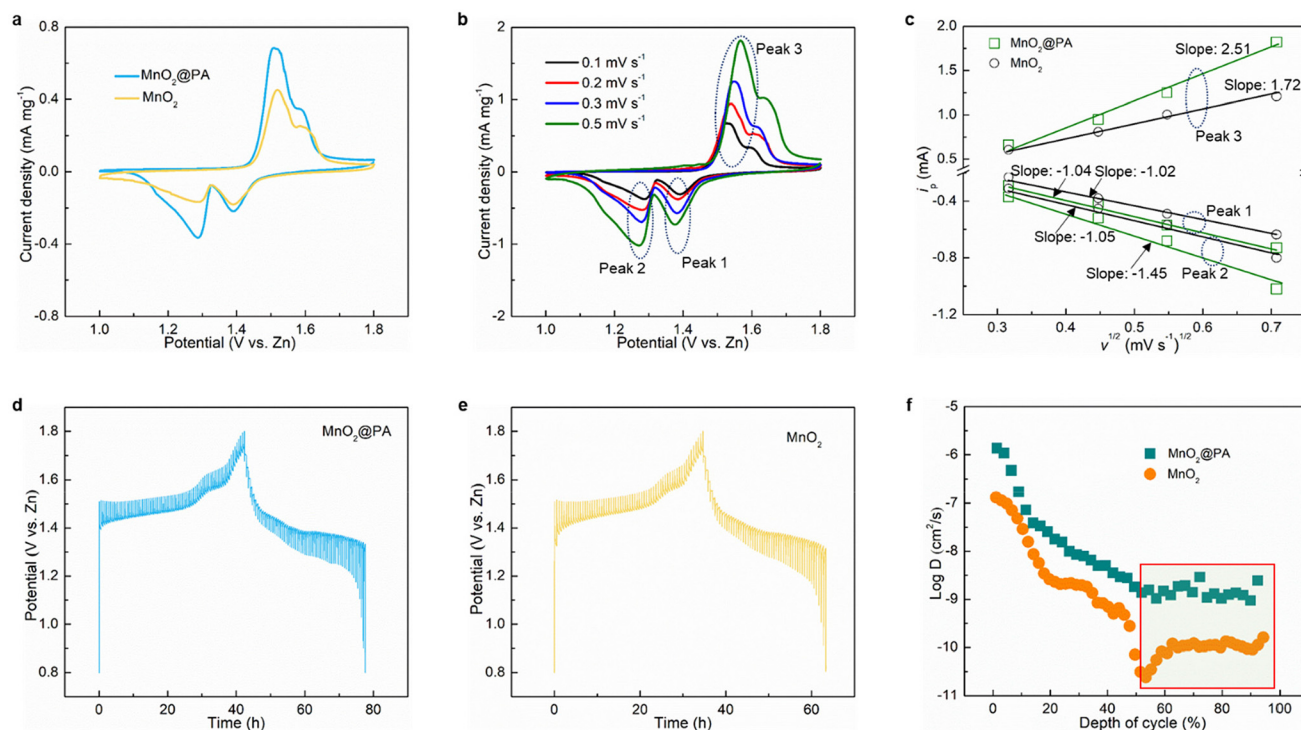


**Fig. 4** Electrochemical reaction kinetics of different cathodes. (a) CV curves for MnO<sub>2</sub> and MnO<sub>2</sub>@PA. (b) CV curves of MnO<sub>2</sub>@PA at various sweep rates. (c) The dependence of log (peak current) on log (scan rate) for obtaining *b* values. Charge/discharge profiles of (d) MnO<sub>2</sub>@PA and (e) MnO<sub>2</sub> during the GITT measurements. (f) The ion diffusion coefficient vs. voltage for MnO<sub>2</sub>@PA and MnO<sub>2</sub> during the 2nd discharge.

composite mixture of nanoparticle aggregations accompanied by structural pulverization (Fig. 5b). As shown in the schematic, this transformation is attributed to the regulatory effect of the PA interlayer. On the one hand, the thin modifier film could accelerate the de-solvation of hydrated zinc ions and facilitate efficient and continuous ion diffusion. On the other hand, the PA layer could shield the MnO<sub>2</sub> matrix from attacks by active water molecules, minimizing the loss of active species and structural collapse to the utmost extent. The results of post-cycling electrode XRD tests further proved that the modified MnO<sub>2</sub> cathode exhibits better cycling performance (Fig. S9†). It is clear that the area of the peak of the by-product Zn<sub>4</sub>SO<sub>4</sub>(OH)<sub>6</sub>·4H<sub>2</sub>O (ZHS) is extensive and the MnO<sub>2</sub> peak is not obvious after cycling of the MnO<sub>2</sub> cathode, which means that the ZHS has become the main loading on the electrode, and the active substance has dissolved in large quantities. In contrast, scanning of the MnO<sub>2</sub>@PA cathode shows that the peak belonging to MnO<sub>2</sub> is still prominent and the intensity of the ZHS peak is relatively small, confirming that the modified MnO<sub>2</sub> has satisfactory stability. Leveraging the modulated interfacial charge transfer and structural protective coating, the Zn-MnO<sub>2</sub>@PA cell demonstrates exceptional energy and cycling performances, as evidenced in Fig. 5c. Notably, the MnO<sub>2</sub>@PA cathode maintains a capacity retention of approximately 73% after 500 charging/discharging cycles at 1 A g<sup>-1</sup>. In contrast, the capacity retention of the unmodified MnO<sub>2</sub> cathode is only 14%. ICP-MS test results further demon-

strate the excellent protective effect of the PA layer, as shown in Table S1.† In the electrolyte of the Zn-MnO<sub>2</sub> beaker battery after cycling, a notable presence of the manganese element is evident, suggesting that the electrode material undergoes partial dissolution during the cycling process, which can significantly impair its performance. Conversely, the post-cycling Zn-MnO<sub>2</sub>@PA beaker cell showed no substantial detection of phosphorus and manganese elements, highlighting the effective protective role of the PA layer. Similarly, an in-depth examination of the positive electrode is of paramount importance. Therefore, the cycling performance of MnO<sub>2</sub>@PA was further evaluated with different N/P ratios, as shown in Fig. S10.† It is evident that the N/P ratio of 1.2 showed the optimum electrochemical performance. It is particularly important to note that the effect of the N/P ratio on cycling stability is significant. Scanning electron microscopy images of the positive electrodes were then obtained after cycling the Zn-MnO<sub>2</sub> and Zn-MnO<sub>2</sub>@PA cells, as shown in Fig. S11.† The unmodified Zn-MnO<sub>2</sub> anode showed obvious cracking and inhomogeneity after 200 cycles, in contrast to the modified Zn-MnO<sub>2</sub>@PA battery anode, which remained chemically stable throughout. This is related to the good adsorption of active water in the water shell by the cathode-modified layer, which reduces the erosion of active water on the anode surface and provides a stable environment for the stripping and deposition of zinc ions. As a proof of concept, a pouch cell employing the MnO<sub>2</sub>@PA cathode was prepared and its cycling stability is



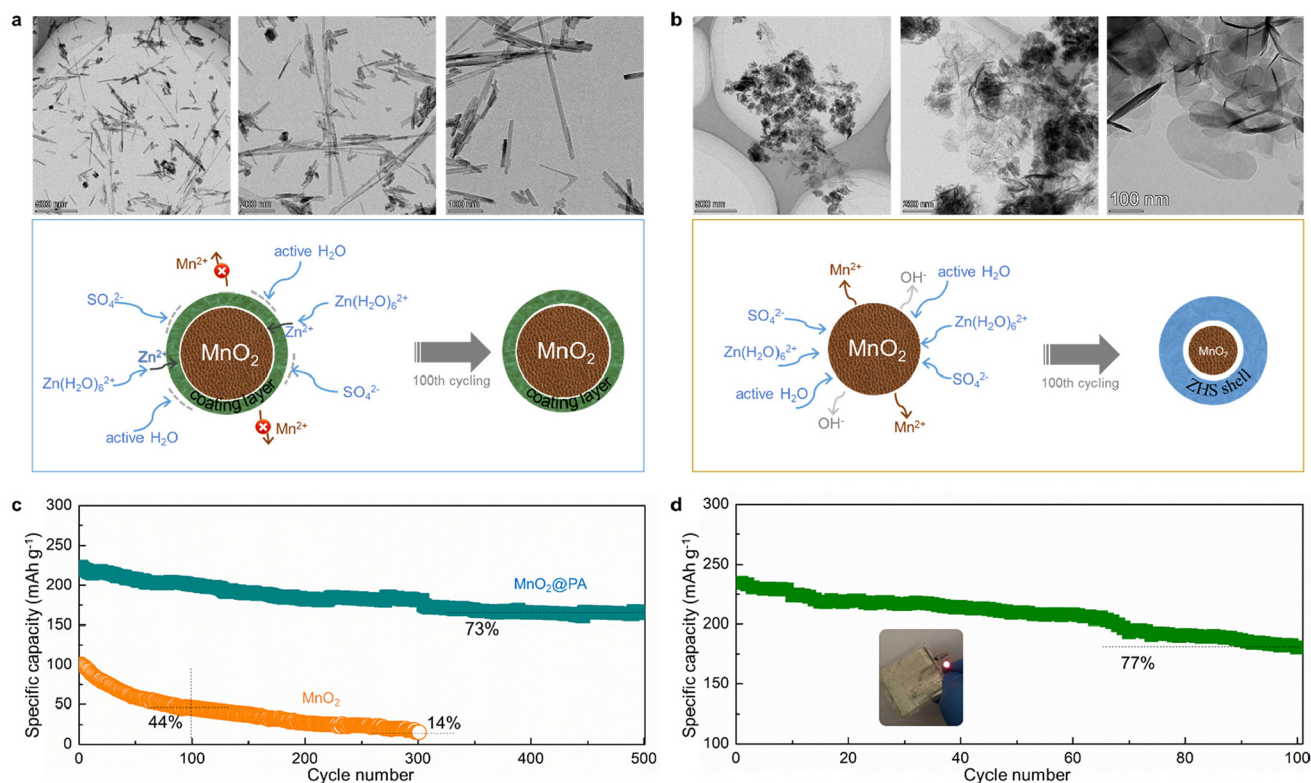


**Fig. 5** Degradation mechanism and cycling stability of Zn-MnO<sub>2</sub> cells assembled with modified MnO<sub>2</sub> cathodes. TEM images of cycled (a) MnO<sub>2</sub>@PA and (b) MnO<sub>2</sub> cathodes; the schematic of the structural evolution of MnO<sub>2</sub> cathodes after a long cycling test, where the formation and aggregation of ZHS accelerate the degradation of metal oxide cathodes. (c) Long-term cycling performance after various cycling numbers. (d) Cycling stability of the flexible Zn-MnO<sub>2</sub> cell, and (inset) a red LED powered by the tandem battery device.

depicted in Fig. 5d. As anticipated, the pouch cell showcases a high energy density of 300 W h kg<sup>-1</sup> (136 W h kg<sup>-1</sup> based on the total weight of electrode materials, as illustrated in Fig. S12†) along with high-capacity retention after 100 cycles. The pouch cell also exhibits the capability to power a red LED (Fig. 5d, inset), emphasizing the potential for future applications of these modified cathodes.

## Conclusion

In summary, we introduce a simplified approach to interfacial engineering that enables the *in situ* construction of a multi-functional modification layer on the surface of an MnO<sub>2</sub> cathode. The phytic acid layer is wrapped around the substrate with strong chemical bonds, which can inhibit the dissolution of phytic acid in the electrolyte, while stabilizing the structure of MnO<sub>2</sub> to reduce the dissolution of Mn<sup>2+</sup>, enhancing cathode stability during cycling. Moreover, the enhanced adsorption of positive ions and accelerated de-solvation process of interfacial hydrated Zn<sup>2+</sup> are achieved by the PA layer with its intrinsic negative charge and superhydrophilicity, which effectively increased the diffusion rate of Zn<sup>2+</sup>, improved its intercalation capacity and achieved a smooth transition during the capacity-dominated intercalation ion transition, effectively reducing the potential difference during the transition. Our experimental

results highlight the effectiveness of the modified interface in creating a solvation structure with low water content for Zn<sup>2+</sup>. As a result, this Zn/MnO<sub>2</sub>@PA cell achieves a specific capacity of 273 mA h g<sup>-1</sup> at a current density of 0.1 A g<sup>-1</sup>, with zinc intercalation capacity exceeding 60%, and retains a specific capacity of 197 mA h g<sup>-1</sup> even when the current density is increased by 10 times. Additionally, a proof-of-concept Zn-ion pouch cell demonstrates an impressive energy density of 300 W h kg<sup>-1</sup> and maintains 77% capacity retention after 100 cycles. This study provides a facile method to accelerate the de-solvation process of hydrated Zn<sup>2+</sup> on the surface of manganese dioxide, thus overcoming its slow kinetics and low capacity in aqueous zinc-ion batteries.

## Data availability

The data that support the findings of this study are included in the published article and its ESI.† These data are also available from the corresponding authors upon request.

## Additional information

Supplementary Information ESI accompanies this paper in the online version of the paper.

## Conflicts of interest

The authors declare no competing financial interests.

## Acknowledgements

This work was financially supported by the Natural Science Foundation of China (22208335, 22109001), the Opening Project of the State Key Laboratory of Polymer Materials Engineering (Sichuan University) (sklpme2024-1-08), the Postdoctoral Fellowship Program of CPSF (GZB20230950), and the China Postdoctoral Science Foundation (2024M754163).

## References

- 1 J. Huang, Z. Wang, M. Hou, X. Dong, Y. Liu, Y. Wang and Y. Xia, *Nat. Commun.*, 2018, **9**, 2906.
- 2 S. Chen, D. Ji, Q. Chen, J. Ma, S. Hou and J. Zhang, *Nat. Commun.*, 2023, **14**, 3526.
- 3 L. Cao, D. Li, T. Pollard, T. Deng, B. Zhang, C. Yang, L. Chen, J. Vatamanu, E. Hu, M. J. Hourwitz, L. Ma, M. Ding, Q. Li, S. Hou, K. Gaskell, J. T. Fourkas, X.-Q. Yang, K. Xu, O. Borodin and C. Wang, *Nat. Nanotechnol.*, 2021, **16**, 902–910.
- 4 Q. Zhang, J. Luan, L. Fu, S. Wu, Y. Tang, X. Ji and H. Wang, *Angew. Chem., Int. Ed.*, 2019, **58**, 15841–15847.
- 5 M. Rana, N. Alghamdi, X. Peng, Y. Huang, B. Wang, L. Wang, I. R. Gentle, S. Hickey and B. Luo, *Exploration*, 2023, **3**, 20220073.
- 6 H. Huang, X. Xia, J. Yun, C. Huang, D. Li, B. Chen, Z. Yang and W. Zhang, *Energy Storage Mater.*, 2022, **52**, 473–484.
- 7 H. J. Chang, I. A. Rodriguez-Perez, M. Fayette, N. L. Canfield, H. Pan, D. Choi, X. Li and D. Reed, *Carbon Energy*, 2021, **3**, 473–481.
- 8 L. Cao, D. Li, E. Hu, J. Xu, T. Deng, L. Ma, Y. Wang, X.-Q. Yang and C. Wang, *J. Am. Chem. Soc.*, 2020, **142**, 21404–21409.
- 9 Z. Liu, C. Liu, Z. Chen, H. Huang, Y. Liu, L. Xue, J. Sun, X. Wang, P. Xiong and J. Zhu, *Exploration*, 2023, **3**, 20220061.
- 10 F. Mo, G. Liang, Q. Meng, Z. Liu, H. Li, J. Fan and C. Zhi, *Energy Environ. Sci.*, 2019, **12**, 706–715.
- 11 P. Sun, L. Ma, W. Zhou, M. Qiu, Z. Wang, D. Chao and W. Mai, *Angew. Chem., Int. Ed.*, 2021, **60**, 18247–18255.
- 12 Y. Ren, F. Meng, S. Zhang, B. Ping, H. Li, B. Yin and T. Ma, *Carbon Energy*, 2022, **4**, 446–457.
- 13 L. Ding, L. Wang, J. Gao, T. Yan, H. Li, J. Mao, F. Song, S. Fedotov, L.-Y. Chang, N. Li, Y. Su, T. Liu and L. Zhang, *Adv. Funct. Mater.*, 2023, **33**, 2301648.
- 14 Z. Shang, S. Wang, H. Zhang, W. Zhang, S. Lu and K. Lu, *Nanoscale*, 2022, **14**, 14433–14454.
- 15 W. Sun, F. Wang, S. Hou, C. Yang, X. Fan, Z. Ma, T. Gao, F. Han, R. Hu, M. Zhu and C. Wang, *J. Am. Chem. Soc.*, 2017, **139**, 9775–9778.
- 16 Z. Shang, H. Zhang, M. Wang, Q. Chen and K. Lu, *Nanoscale*, 2022, **14**, 6085–6093.
- 17 Y. Zeng, X. Zhang, Y. Meng, M. Yu, J. Yi, Y. Wu, X. Lu and Y. Tong, *Adv. Mater.*, 2017, **29**, 1700274.
- 18 A. Zhang, R. Zhao, Y. Wang, J. Yue, J. Yang, X. Wang, C. Wu and Y. Bai, *Angew. Chem., Int. Ed.*, 2023, **62**, e202313163.
- 19 N. Zhang, F. Cheng, J. Liu, L. Wang, X. Long, X. Liu, F. Li and J. Chen, *Nat. Commun.*, 2017, **8**, 405.
- 20 W. Xu, K. Zhao, W. Huo, Y. Wang, G. Yao, X. Gu, H. Cheng, L. Mai, C. Hu and X. Wang, *Nano Energy*, 2019, **62**, 275–281.
- 21 X. Xiao, L. Zhang, W. Xin, M. Yang, Y. Geng, M. Niu, H. Zhang and Z. Zhu, *Small*, 2024, **20**, 2309271.
- 22 H. Yang, T. Zhang, D. Chen, Y. Tan, W. Zhou, L. Li, W. Li, G. Li, W. Han, H. J. Fan and D. Chao, *Adv. Mater.*, 2023, **35**, 2300053.
- 23 Y. Chen, Z. Deng, Y. Sun, Y. Li, H. Zhang, G. Li, H. Zeng and X. Wang, *Nano-Micro Lett.*, 2024, **16**, 96.
- 24 X. Gao, K. Lu, L. Xu, H. Xu, H. Lu, F. Gao, S. Hou and H. Ma, *Nanoscale*, 2016, **8**, 1555–1564.
- 25 X. Gao, H. Zhang, X. Liu and X. Lu, *Carbon Energy*, 2020, **2**, 387–407.
- 26 S. Gao, B. Li, K. Lu, S. Alabidun, F. Xia, C. Nickel, T. Xu and Y. Cheng, *ACS Appl. Mater. Interfaces*, 2021, **13**, 23724–23731.
- 27 K. Lu, Z. Hu, Z. Xiang, J. Ma, B. Song, J. Zhang and H. Ma, *Angew. Chem., Int. Ed.*, 2016, **55**, 10448–10452.
- 28 B. Luo, Y. Wang, L. Sun, S. Zheng, G. Duan, Z. Bao, Z. Ye and J. Huang, *J. Energy Chem.*, 2023, **77**, 632–641.
- 29 Z. J. Liu, G. J. Li, M. R. Xi, Y. D. Huang, H. B. Li, H. Y. Jin, J. Ding, S. L. Zhang, C. F. Zhang and Z. P. Guo, *Angew. Chem., Int. Ed.*, 2024, **63**, e202319091.
- 30 M. Zhou, Y. Chen, G. Fang and S. Liang, *Energy Storage Mater.*, 2022, **45**, 618–646.
- 31 T. Zhang, Y. Tang, G. Fang, C. Zhang, H. Zhang, X. Guo, X. Cao, J. Zhou, A. Pan and S. Liang, *Adv. Funct. Mater.*, 2020, **30**, 2002711.
- 32 H. Yang, D. Chen, R. Zhao, G. Li, H. Xu, L. Li, X. Liu, G. Li, D. Chao and W. Han, *Energy Environ. Sci.*, 2023, **16**, 2910–2923.
- 33 H. Zhang, M. Wang, B. Song, X.-L. Huang, W. Zhang, E. Zhang, Y. Cheng and K. Lu, *Angew. Chem., Int. Ed.*, 2024, **63**, e202402274.
- 34 T. Xiong, Z. G. Yu, H. Wu, Y. Du, Q. Xie, J. Chen, Y.-W. Zhang, S. J. Pennycook, W. S. V. Lee and J. Xue, *Adv. Energy Mater.*, 2019, **9**, 1803815.
- 35 X. Zeng, J. Lin, W. Cai, Q. Lu, S. Fu, J. Li, X. Yan, X. Wen, C. Zhou and M. Zhang, *Chemosphere*, 2021, **264**, 128395.
- 36 Y. Wang, M. Liu, C. Hu, Y. Xin, D. Ma, M. Gao and H. Xie, *Chem. Eng. J.*, 2022, **433**, 134048.
- 37 W. Tian, D. Cheng, S. Wang, C. Xiong and Q. Yang, *Appl. Surf. Sci.*, 2019, **495**, 143589.
- 38 Z. Shen, J. Mao, G. Yu, W. Zhang, S. Mao, W. Zhong, H. Cheng, J. Guo, J. Zhang and Y. Lu, *Angew. Chem.*, 2023, **135**, e202218452.



- 39 O. Oll, T. Romann, C. Siimenson and E. Lust, *Electrochem. Commun.*, 2017, **82**, 39–42.
- 40 K. Lu, H. Zhang, B. Song, W. Pan, H. Ma and J. Zhang, *Electrochim. Acta*, 2019, **296**, 755–761.
- 41 B. Lee, H. R. Seo, H. R. Lee, C. S. Yoon, J. H. Kim, K. Y. Chung, B. W. Cho and S. H. Oh, *ChemSusChem*, 2016, **9**, 2948–2956.
- 42 C. Li, R. Kingsbury, L. Zhou, A. Shyamsunder, K. A. Persson and L. F. Nazar, *ACS Energy Lett.*, 2022, **7**, 533–540.
- 43 K. Lu, B. Song, Y. Zhang, H. Ma and J. Zhang, *J. Mater. Chem. A*, 2017, **5**, 23628–23633.
- 44 Y. Ding, L. Yin, T. Du, Y. Wang, Z. He, J. A. Yuwono, G. Li, J. Liu, S. Zhang, T. Yang and Z. Guo, *Adv. Funct. Mater.*, 2024, **34**, 2314388.
- 45 M.-C. Han, J.-H. Zhang, C.-Y. Yu, J.-C. Yu, Y.-X. Wang, Z.-G. Jiang, M. Yao, G. Xie, Z.-Z. Yu and J. Qu, *Angew. Chem., Int. Ed.*, 2024, **63**, e202403695.
- 46 F. Li, D. Ma, K. Ouyang, M. Yang, J. Qiu, J. Feng, Y. Wang, H. Mi, S. Sun, L. Sun, C. He and P. Zhang, *Adv. Energy Mater.*, 2023, **13**, 2204365.
- 47 J. H. Park, C. Choi, J. B. Park, S. Yu and D.-W. Kim, *Adv. Energy Mater.*, 2023, **14**, 2302493.